Ultramicroscopy 161 (2016) 119–129

Contents lists available at ScienceDirect

Ultramicroscopy

journal homepage: www.elsevier.com/locate/ultramic

Full Length Article

Large volume serial section tomography by Xe Plasma FIB dual beam microscopy

T.L. Burnett [a,b], R. Kelley [c], B. Winiarski [a,b], L. Contreras [c], M. Daly [a], A. Gholinia [a], M.G. Burke [a], P.J. Withers [a,d,*]

[a] School of Materials, University of Manchester, Manchester M13 9PL, UK
[b] FEI Company, Achtseweg Noord 5, Bldg, 5651 GG, Eindhoven, The Netherlands
[c] FEI Company, 5350 NE Dawson Creek Drive, Hillsboro, OR 97124, United States
[d] BP International Centre for Advanced Materials, University of Manchester, Manchester M13 9PL, UK

ARTICLE INFO

Article history:
Received 5 June 2015
Received in revised form
28 September 2015
Accepted 6 November 2015
Available online 10 November 2015

Keywords:
Xe^+ Plasma FIB-SEM dual beam microscope
Scanning electron microscopy
3D imaging
X-ray micro-tomography (micro-CT)
A508 grade 3 steel

ABSTRACT

Ga^+ Focused Ion Beam-Scanning Electron Microscopes (FIB-SEM) have revolutionised the level of microstructural information that can be recovered in 3D by block face serial section tomography (SST), as well as enabling the site-specific removal of smaller regions for subsequent transmission electron microscope (TEM) examination. However, Ga^+ FIB material removal rates limit the volumes and depths that can be probed to dimensions in the tens of microns range. Emerging Xe^+ Plasma Focused Ion Beam-Scanning Electron Microscope (PFIB-SEM) systems promise faster removal rates. Here we examine the potential of the method for large volume serial section tomography as applied to bainitic steel and WC–Co hard metals. Our studies demonstrate that with careful control of milling parameters precise automated serial sectioning can be achieved with low levels of milling artefacts at removal rates some 60× faster. Volumes that are hundreds of microns in dimension have been collected using fully automated SST routines in feasible timescales (< 24 h) showing good grain orientation contrast and capturing microstructural features at the tens of nanometres to the tens of microns scale. Accompanying electron back scattered diffraction (EBSD) maps show high indexing rates suggesting low levels of surface damage. Further, under high current Ga^+ FIB milling WC–Co is prone to amorphisation of WC surface layers and phase transformation of the Co phase, neither of which have been observed at PFIB currents as high as 60 nA at 30 kV. Xe^+ PFIB dual beam microscopes promise to radically extend our capability for 3D tomography, 3D EDX, 3D EBSD as well as correlative tomography.

1. Introduction

A great deal of information about the three dimensional (3D) nature of materials can be obtained by the analysis of orthogonal 2D sections, but there are many cases where full 3D characterization is required. For example, when evaluating the interconnectedness of various types of networks, such as pores in fuel cell materials [1], vasculature in biological systems [2], corrosion ingress [3] as well as the complex morphology of percolating two phase systems [4]. Non-destructive techniques such as X-ray computed tomography (CT), positron emission tomography (PET) and nuclear magnetic resonance imaging (MRI) all offer 3D imaging capability. Furthermore, by repeatedly acquiring images they enable time-lapse CT, so-called 4D studies [5,6]. These techniques, however, are limited both in terms of spatial resolution and in the types of contrast they can provide.

Consequently, imaging across multiple length scales often relies upon scanning and transmission electron microscopies (SEM and TEM respectively) to provide information at sub-micron scales. In cases where high spatial resolution information is required in 3D, serial sectioning routines have been successfully applied to collect stacks of 2D images which can be aligned in sequence to build up a 3D image of the specimen. Sectioning methods vary according to the slicing methodology and the imaging technique employed, including; mechanical polishing and optical imaging [7], ultramicrotomy [8], laser machining [9], Broad Ar^+ Ion Beam (BIB)[1] milling [10,11] or Ga^+ FIB[2] machining [12,13] and SEM imaging (Fig. 1). Dual beam FIB-SEM

* Corresponding author at: School of Materials, University of Manchester, Manchester M13 9PL, UK.
E-mail address: P.J.Withers@manchester.ac.uk (P.J. Withers).

[1] Hereafter abbreviation BIB refers to Ar^+ BIB.
[2] Hereafter abbreviation FIB refers to Ga^+ FIB with liquid metal ion source (LMIS).

http://dx.doi.org/10.1016/j.ultramic.2015.11.001

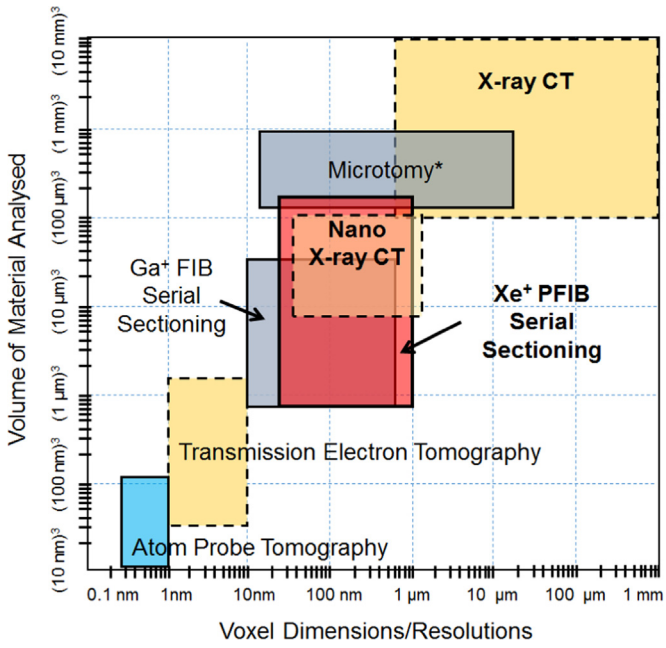

Fig. 1. 3D imaging methods for materials science (non-destructive methods represented by dashed lines; * – for soft materials only), after [18].

microscopes in particular have become very popular because they allow both high-resolution imaging and flexible micromachining within a single instrument facilitating automated workflows. The 3D analysis can be further extended down to sub-nanometer resolution through the use of TEM tomography [14,15] and atom probe tomography [16,17].

Recently correlative tomography has been proposed [19] aimed at following the same volume of interest (VoI) across multiple scales and imaging modalities in much the same way that correlative microscopy has been applied to surface imaging [20]. From this viewpoint the FIB-SEM is important because it enables the site-specific extraction of volumes identified by non-destructive 3D imaging techniques (e.g. X-ray CT) for subsequent higher resolution examination. However, as is evident from Fig. 1 the FIB provides access only to depths and volumes of interest tens of microns in dimension.

Consequently there is a need for a tool with the site-specific precision of a FIB, but with the ability to excavate and serial section larger volumes. Laser techniques are capable of much faster material removal rates and can excise millimetre-sized regions, however, the surface damage induced by the laser often requires a subsequent polish with a FIB or BIB prior to microstructural examination [9,21]. Nevertheless, for millimetre-sized volumes laser-based methods are likely to emerge as the tool of choice. Plasma Xe^+ FIBs[3] have been employed for some time, especially in the electronics industry, for milling materials at the hundreds of micron length scale [22–28]. Recently plasma focused ion beams have been coupled with scanning electron microscopes to form so-called PFIB-SEM dual beam microscopes [29], but to-date their capabilities and applications have not been systematically reported in the archival literature.

There are many possible ion beam chemistries and source types that can be applied [30]. Here our discussion is limited to the magnetically enhanced inductively-coupled Xenon plasma ion source (ICP) [30]. The ability of a two lens ion beam column is limited to a demagnification of the source by ~200 × to provide a focussed ion beam means that it is largely the characteristics of the source (virtual) spot size that will determine the final beam diameter. Fig. 2b shows the spot size (d_{50}) as a function of the beam current [26] and shows that for currents, I, above ~60 nA the spot size for the PFIB is smaller than that of the Ga^+ liquid metal ion source (LMIS), meaning that for the same focussing optics, a finer PFIB spot can be achieved. The small and divergent nature of the LMIS source means that at higher currents the spot size is dominated by spherical aberration resulting in a non-Gaussian beam shape with large tails. The result is that for currents greater than 5 nA the spot size increases significantly. The Xe^+ ICP source is broader but collimated, such that it demonstrates superior angular intensity compared to the Ga^+ LMIS, making it more suitable for high current milling as the effects of spherical aberration are not realised [26,31]. This makes the attainment of currents in the μA range possible which is not possible with a LMIS whilst retaining a focussed beam (See Fig. 2b). (NB: LMIS is capable of spot sizes < 5 nm and for the Xe^+ ICP ~20 nm has been demonstrated [32]). Another important factor is the efficiency of sputtering in the PFIB compared with the FIB. Previous work (see Table 1) has quantified the difference in sputter rates when comparing the Ga^+ to the Xe^+ beams for a range of materials via experiment and Stopping and Range of Ions in Matter (SRIM) modelling [33,34]. The general trend is for moderately (10–30%) higher sputter rates per coulomb for the Xe^+ compared to the Ga^+ beam. Of particular note is the ~300% higher sputter rates for Cu and 30–50% higher sputter rates for Si by the Xe^+ beam compared to the Ga^+ beam. GaAs is the exception to this trend, for the materials investigated, showing higher sputter rates for Ga^+. The result is that the same current will generally lead to somewhat higher removal rates when using Xe^+. The SRIM results capture the fact that Xe^+ is a more massive ion than the Ga^+ and results in more atoms of material ejected from the target per incident ion. SRIM also indicates a shallower depth of penetration of the Xe^+ ions, for example the penetration of Ga^+ and Xe^+ in Si is 24 nm and 28 nm respectively at 30 kV.

Clearly faster milling rates are not advantageous if the milling damage requires additional polishing steps. Previous studies on silicon at glancing angle incidence have shown that the depth of damage introduced by the Xe^+ Plasma FIB in silicon created 20–40% less damage than that measured from a Ga^+ FIB prepared surface [35]. The depth of amorphous damage was recorded as ~22 nm at 30 kV and 3.1 nm at 5 kV for grazing incidence milling using Ga^+ FIB and ~13 nm at 30 kV and 2.4 nm at 5 kV using Xe^+ FIB measured in the TEM (see Fig. 3).

Electron backscatter diffraction (EBSD) information is only generated from a depth of a few tens of nanometres and is notoriously sensitive to the surface condition [36] and thus EBSD quality can provide a good indicator of beam damage. Recent EBSD results [24] suggest that the PFIB is capable of producing a good quality surface indicative of low damage milling.

It is clear that for Ga^+ milling, in addition to the physical damage that is imparted into the material, there is also the possibility of chemical interactions, most notably the formation of intermetallic phases. For example Cu_3Ga [37] and the well-known grain boundary embrittlement of Al alloys [38,39]. The noble nature of the Xe^+ discounts this possibility and as such makes it an attractive alternative to Ga^+ for materials which are chemically sensitive to Ga^+ e.g. Al, Cu and Ga containing materials.

The reality is that for the creation of cross sections and TEM lamellae normal incidence milling of the samples is always avoided where possible and protective metallic layers employed where this is not possible [40]. This approach of grazing incidence milling has repeatedly shown that the depth of damage can be reduced to practically negligible levels with the use of low kV polishing completing the process [41].

Lastly the creation of largely artefact-free deep cross sections

[3] Hereafter PFIB refers to Plasma Xe^+ FIB microscope with Inductively Coupled Plasma gun (ICP).

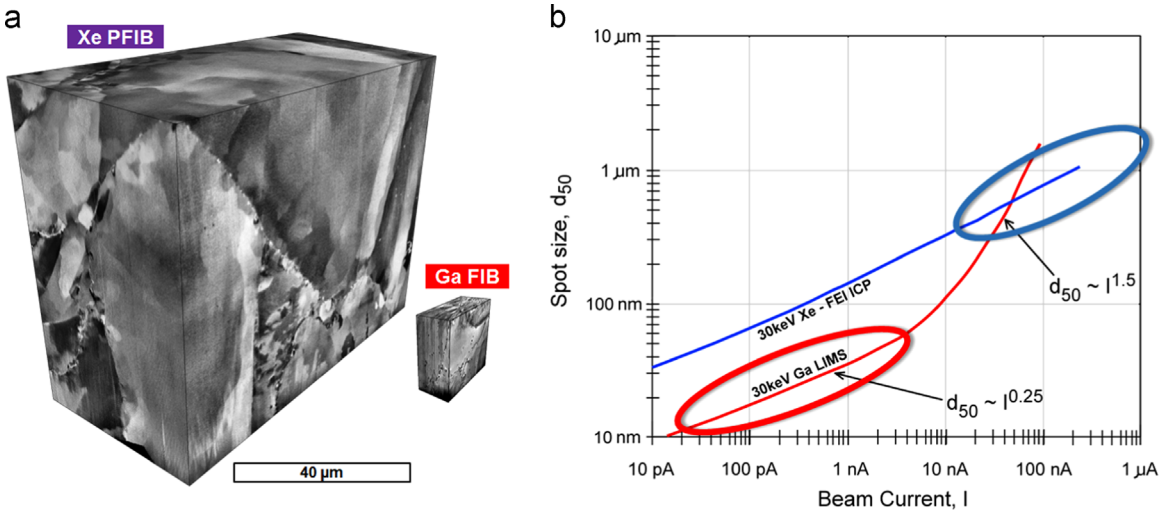

Fig. 2. (a) 3D serial section volumes of a stainless steel collected using the PFIB-SEM (59 nA at 30 kV, 100 nm slice thickness) and a FIB-SEM (1 nA at 30 kV, 25 nm slice thickness) in similar times, (b) Comparison of the spot size, d_{50}, as a function of the beam current, I, for Ga FIB and Xe PFIB [26]. d_{50} is the beam width containing 50% of the beam current.

Table 1
Measured and modelled sputter rates for Ga^+ and Xe^+ ion beams at 30 kV.

Material	Sputter rate measured (μm^3/nC)		Sputter rates calculated from SRIM (μm^3/nC)	
	Ga^+	**Xe^+**	**Ga^+**	**Xe^+**
Diamond	0.09	0.11	0.07	0.09
Si	0.22–0.27	0.35–0.42	0.27	0.37
Al	0.31	0.41	0.37	0.5
Ti	0.31	0.32	0.26	0.28
GaAs	0.86	0.61	1.45	1.61
Cu	0.15–0.55	1.1–1.6	0.69	0.85
Epoxy resin	0.3	0.31	–	–

has been demonstrated by Kwakman et al. [25], showing that good surface quality can be achieved using the PFIB in combination with a rocking milling technique (the rocking milling routine is described in detail in Section 2.3). In essence; the rocking polish replaces milling from a top–down (vertical) direction, as commonly employed in the FIB, and employs two different milling directions a few degrees either side of the vertical milling direction applied for alternate slices. Rocking milling has also been shown to reduce the roughness of the surface from ~400 nm RMS[4] to 50 nm RMS for a 150 µm deep cross section of a copper through silicon via (TSV) [24], as measured by atomic force microscopy.

In summary, work to date has shown that a combination of the higher currents available for the PFIB, the generally higher sputter rates and the reduced physical and chemical damage has meant that it is possible to achieve 20–60 × faster milling compared to the FIB [24,42].

Herein we explore the potential of PFIB milling for the acquisition of large (> 100 µm) 3D volumetric datasets using one of the first FEI Helios PFIB dual beam microscopes. We present a comparison of cross section preparation for a well-characterised hard metal (WC-11 wt% Co), known to be a difficult material to prepare using conventional Ga^+ FIB milling [4]. We discuss in detail the EBSD results recorded from the PFIB prepared cross sections of the hard metal compared directly with results on FIB prepared slices collected on the same region of interest and under the same EBSD conditions. Secondly we present large volume serial block face sectioning results for the microstructural examination of defects, grain structures and fine carbides for a sample excavated from near the fracture surface from a fractured sample of an A508 Grade 3 reactor pressure vessel steel. Finally we look at the potential of the PFIB-SEM for correlative tomography. Consideration of the process and low kV polishing conditions pertinent for TEM preparation is not discussed explicitly here.

[4] RMS – Root Mean Square.

2. Experimental

2.1. Materials

A WC–Co hard metal was selected to study Xe^+ induced damage because previous experience has shown that WC–Co is a difficult material to Ga^+ FIB mill due to beam induced amorphization of the WC surface (affecting the electron backscatter diffraction (EBSD) pattern quality) and a propensity for the Co phase to transform under the beam [4,12]. It has been carefully characterised previously by conventional milling techniques including mechanical polishing [4], FIB [4,12] and BIB [4,10,11] polishing. A WC–Co hard metal containing 11 mass% Co was produced by Marshalls Hard Metals Ltd. using conventional powder metallurgical methods involving both solid state and liquid phase sintering giving coarse WC grains, the grains range in size from 1–15 µm [10,11]. The grains of the binder Co phase extend over much larger distances than the size of the WC particles, sometimes up to 1 mm in size [43] creating complex grain geometries.

In order to examine the 3D imaging capability a core taken from the fracture surface of a compact tension sample of A508 Grade 3 pressure vessel reactor steel [44] was examined. The sample failed due to ductile tearing. The prepared core captured the fracture surface at one end and material below the fracture surface for the full thickness of the compact tension specimen. X-ray computed tomography (CT) has previously been used to characterize large cavities > 10 µm in width and the PFIB was applied to provide higher resolution tomography to measure the distribution of finer pores.

2.2. Sample preparation and data acquisition set up

An FEI Helios PFIB Dual Beam FIB-SEM was used at an accelerating voltage of 30 kV for all experiments. A new version (1.6) of

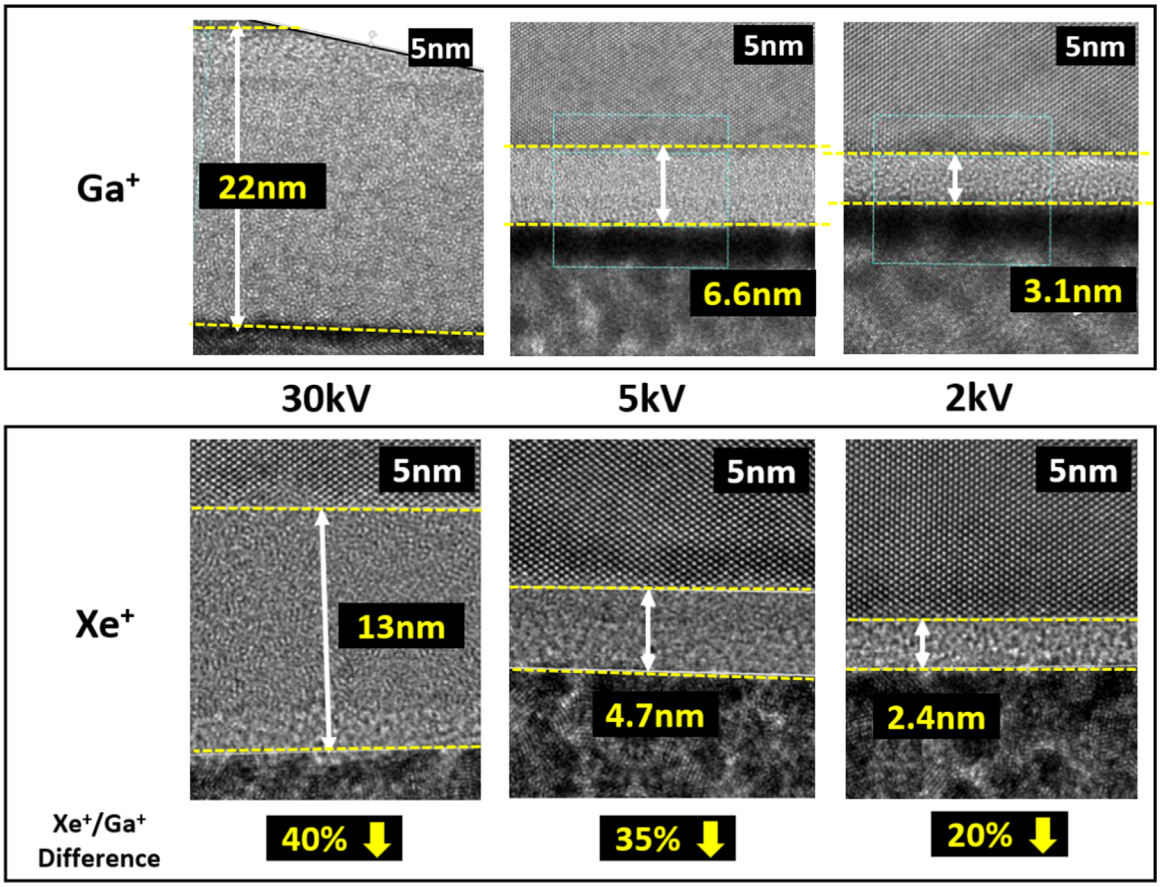

Fig. 3. TEM images showing the depth of amorphization of Si prepared at 30 kV, 5 kV and 2 kV comparing results from Xe^+ and Ga^+ FIB at 30 kV, 5 kV and 2 kV [35].

the FEI Slice and View™ software which incorporates a rocking polish (described in Section 2.3) in to an automated routine was used for the serial sectioning. All EBSD data was recorded using Oxford Instruments NordlysNano EBSD detector and Aztec software.

3D visualization of the serial section and X-ray CT data was conducted using Avizo 9.0.0 software.

The cross-section of the WC-11 wt% Co sample for EBSD analysis was also prepared using PFIB at 59 nA and 30 kV but without the rocking polish to maintain a fair comparison with the FIB prepared cross sections. Surfaces for EBSD mapping of the same WC-11 wt% Co sample were also prepared using an FEI Nova NanoLab FIB using a Ga^+ LMIS source at 30 kV and currents of 20 nA and 1 nA. To provide a benchmark for comparison a Gatan Ilion Ar^+ Broad Ion Beam (BIB) Precision Polishing and Etching System (PECS) was also used to prepare a surface of the WC-11% Co sample by removing ~250 nm of material. A three-step polishing procedure in 2×10^{-3} Pa vacuum used a range of BIB conditions: (i) 610 μA at 10 kV for 32 min., (ii) 450 μA at 7 kV for 10 min., and finally (iii) 350 μA at 6 kV for 10 min. The sample was rocked continuously by ± 30° at a rate of 12 oscillations/min, with the sample surface exposed to BIB at glancing angle.

For all the differently prepared surfaces of the WC-11 wt% Co sample identical EBSD acquisition parameters were used to allow direct comparisons. EBSD maps were collected at 20 kV, 4 nA current and 14 mm working distance. The following EBSD conditions were used: 50 nm step size, 6 ms dwell time, averaged frames × 1, 4 × 4 binning, 12 bands, RA and Hough = 50 giving an acquisition rate of 164 Hz.

3D serial sectioning was conducted on a block of WC-11 wt%Co hard metal 150 × 120 × 80 μm^3 in size. 790 slices were acquired using the PFIB at 30 kV and 59 nA. Each 100 nm thick slice took 2 min and 12 s to cut. A rocking polish of ±5°, determined experimentally before the actual data collection, was used. SEM images 6144 × 4096 in size were collected using 2 kV and 2.8 nA using the through-lens detector (TLD), giving a pixel size of 30 nm These images were collected with a dwell time = 6 μs and a single frame acquisition taking 3 min per image. Overall it took 65 h to acquire the whole data set making this experiment completely impractical if using the Ga^+ FIB.

For the A508 Grade 3 reactor pressure vessel steel X-ray CT imaging was conducted using a Nikon Metrology 225/320 kV Custom Bay system. The voltage used was 80 kV and the current 130 μA. 3142 projections were acquired with an exposure time of 1 s per projection. The entire volume was reconstructed at full resolution using a FDK reconstruction algorithm associated with the acquisition hardware. The resolution of the reconstructed volume was $(2\ \mu m)^3$.

Using measurements and orientation from the X-ray CT data a site for serial sectioning was prepared using the PFIB to capture a particular region of interest where a large pore ~0.5 mm below the fracture surface could be seen (see Fig. 4a). The methodology to achieve this is described in detail by Burnett et al. [45]. Using 30 kV and a current of 1.3 μA the top as well as the sides and the front of a block were prepared ready for serial sectioning. For the preparation of the top of the block 470 nA and 180 nA were used in sequence to ensure a smooth top surface. 470 nA, 180 nA and finally 59 nA were used to prepare the front of the block face all at 30 kV.

A block of dimensions ~135 μm across and ~115 μm deep of the A508 Grade 3 sample was serial sectioned. A total of 186 slices were recorded with each 80 nm thick slice taking ~6 min 20 s

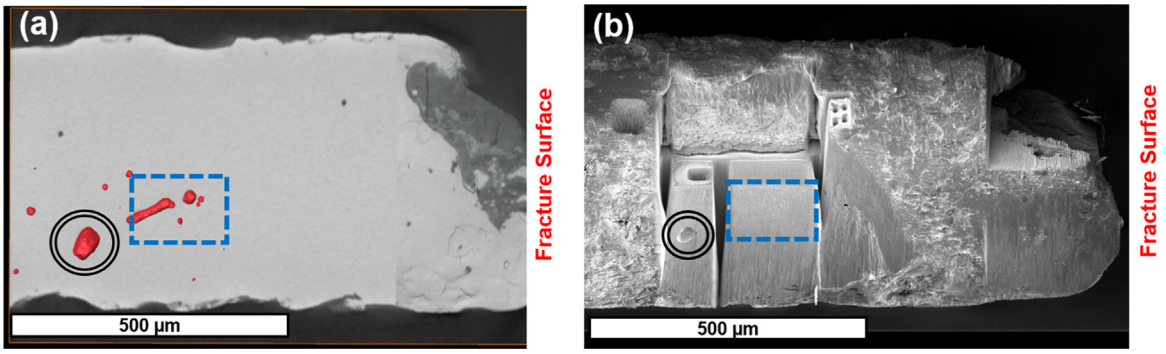

Fig. 4. (a) A virtual section from the X-ray CT data for the 0.5 mm diameter core machined from below a fracture surface caused by ductile fracture of a A508 Grade 3 pressure vessel reactor steel compact tension specimen [32], (b) SEM image showing the same region being prepared by PFIB milling ready for serial sectioning.

with 3 min 25 s for the image acquisition and the remaining 2 min 55 s predominantly milling time and some limited stage move time (<10 s). Serial sectioning of this sample was conducted using 59 nA current and 30 kV acceleration voltage. It was determined experimentally that a beam current of 59 nA was appropriate for serial section milling to obtain a surface finish of sufficient quality to then image the microstructure using the TLD detector. A rocking mill angle of $\pm 4^\circ$ was used (see Section 2.3). SEM images were collected using 2 kV, 800 pA and the through lens detector (TLD), a horizontal field width of 160 μm with a resolution of 6144×4096 gave a pixel size of 26 nm.

Both of the stacks of SEM images acquired from the serial sectioning were aligned using the align slices module using a least squares algorithm in Avizo 9.0.0. The aligned images were filtered using the Fourier Filter (FFT Filter) which removes periodic noise such as the vertical curtaining effects produced from the rocking milling process as such the FFT filter was used at two angles that match the rocking mill angles. A sharpening filter was subsequently applied to compensate for some blurring resulting from the FFT filter. For the A508 Grade 3 data an edge preserving filter and a median filter were then applied to improve the definition of the voids, inclusions and carbides. The data was then segmented using a semi-automated approach which combined a watershed segmentation routine to label the large voids and a top hat segmentation routine to label the carbides, both procedures are incorporated into Avizo 9.0.0 software.

The EBSD map obtained from the A508 Grade 3 steel was acquired using a 20 kV electron beam energy, 4 nA current and 10 mm working distance. The following EBSD conditions were used: 75 nm step size, 2.3 ms dwell time, averaged frames $\times 4$, 4×4 binning, 6 bands, RA and Hough=60 giving an acquisition rate of 95 Hz.

2.3. Serial sectioning procedure

Fig. 5 shows how a region of interest is typically prepared for serial sectioning. The volume of interest is first protected by depositing a protective top layer of (a Pt layer of 100×100 μm^2 and 1 μm thick is deposited with in about 10 minutes) covering the RoI and extending sufficiently far to provide a uniform region where the tracking fiducials can also be milled. A front trench is milled to create a cross section and is accompanied by the excavation of side trenches, which not only define the block for serial sectioning but also control re-deposition during milling. Thus a block of material is defined which is to be serially sectioned. These blocks for serial sectioning are typically prepared with a multistep milling procedure using the PFIB at 30 kV and several beam currents, starting with fast bulk cutting at 1.3 μA, followed by gentler milling at 180 nA to define the final shape. In each case the maximum current that is used to give the required surface finish needs to be determined for each different type of material.

To successively reveal a series of equally spaced and parallel slices, each with the exposed block face undamaged, we have applied and refined the rocking milling process integrated within a fully automated routine. Once a cross-section is prepared (see Fig. 5) in the region of interest rocking milling was used, alternating between $\pm\alpha$ ($-8^\circ \le \alpha \le 8^\circ$) relative to the conventional vertical, top–down, milling. This procedure is illustrated in Fig. 6. To start, the sample was in the imaging position (sample tilted to 52° and 0° rotation) so that the ion beam is incident to the normal

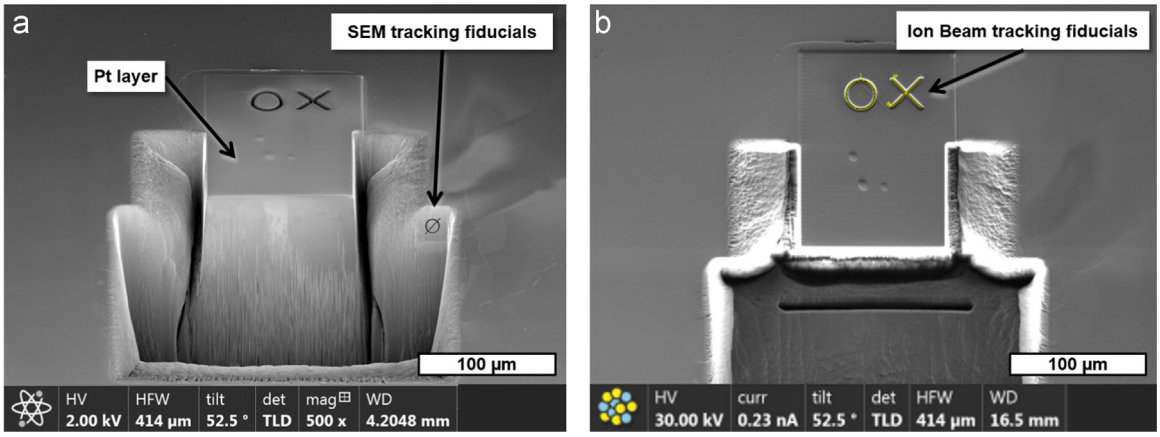

Fig. 5. Typical preparation of a region for serial sectioning tomography data acquisition prepared using the PFIB. A multi-step preparation procedure used the PFIB at 30 kV and 1.3 μA, 180 nA and 59 nA to prepare the block for the serial sectioning. With the sample tilted to 52° and with 0° rotation the block face is presented to the electron beam (a) SEM image and (b) PFIB ion beam image of the same region (a vertical top down view).

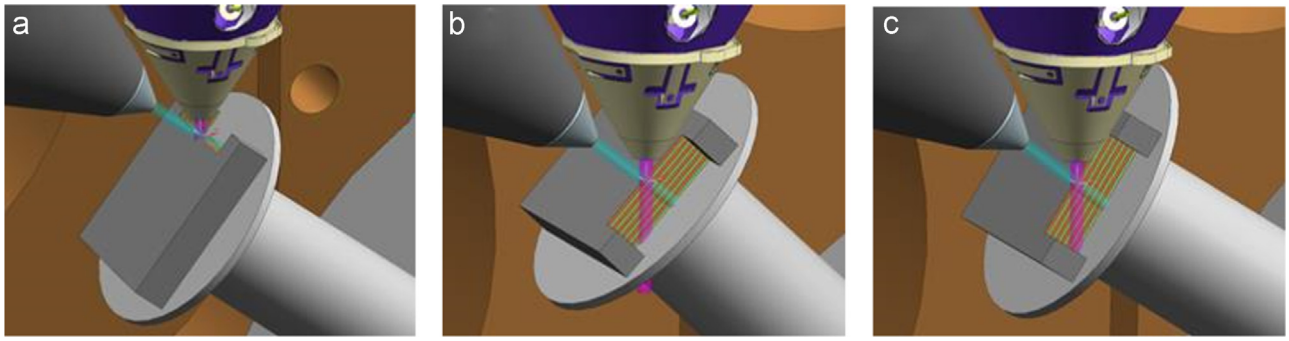

Fig. 6. Rocking Polish Routine explained showing a diagrammatic view inside the FIB-SEM chamber (a) shows the sample in the imaging position of 52° tilt and 0° rotation (b) rotation of 90° and tilt at 47° for the rocking polish step at −5° (c) rotation of 90° and tilt 5° for the rocking polish step at +5°. The magenta beam represents the electron beam and the cyan the ion beam.

of the sample surface and the block face is presented to the electron beam for imaging of the block face (Fig. 6a). The sample was then subjected to a 90° compucentric rotation (i.e. rotation of the sample by 90° around the centre of the image). The sample is then tilted (which due to the rotation is now a tilt parallel to the cross section length), in this example case the sample was then tilted to 47° giving a $\alpha = -5°$ offset (Fig. 6b). The face was milled at this position before returning to the imaging position. After the image of the block face was recorded the sample was rotated to 90° and then tilted to 57° giving the $\alpha = +5°$ offset (Fig. 6c). After milling from this position the stage moved the sample back to the imaging position. This sequence (Fig. 6a) b) a) c) a) b) a) c) ……) was repeated to build up the series of sections.

Within the automated routine ion beam tracking fiducial markers (see Fig. 5) are used and recognised providing the placement of the milling location of the cross-sectional block face slices. To improve accuracy three different images of the fiducials are automatically recorded, one from each of the different tilt positions $\alpha = -5°$, 0° and +5°. This avoids inaccuracies induced by distortion of the fiducial image when recorded from the tilt

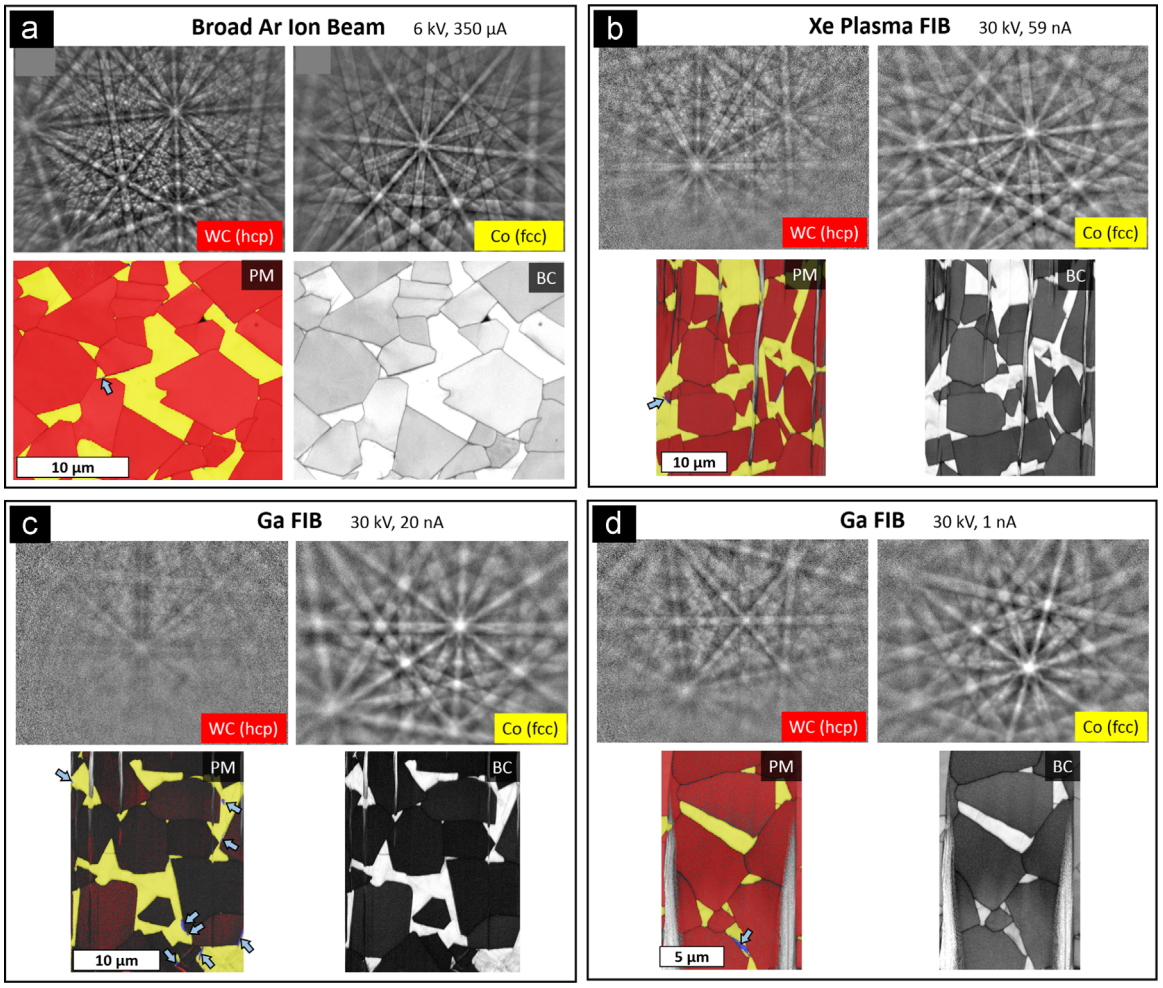

Fig. 7. EBSD results acquired under the same conditions showing representative phase maps (PM), band contrast (BC) maps and raw patterns for WC -11 wt% Co for surfaces prepared by (a) BIB at 6 kV and 350 µA, (b) PFIB at 30 kV and 59 nA, (c) FIB at 30 kV and 20 nA and (d) FIB at 30 kV and 1 nA. The band contrast maps are presented using the same greyscale for comparison. Arrows indicate Co HCP phase.

positions. The FEI Slice and View™ (version 1.6) software incorporates a rocking polish as described above and was used in this work.

3. Results and discussion

3.1. Milling damage study using a WC–Co hard metal sample

Given the susceptibility of WC–Co hard metals to Ga^+ FIB milling damage [4,12], this material has been used to assess the PFIB milling quality. Previously we have found that Ar^+ BIB polishing introduces only low levels of damage into this system [10,11] and so it is used as a benchmark here. The electron backscatter diffraction patterns generated from the Ar^+ BIB prepared surface (Fig. 7a) are very high quality with high indexing rates (90%) for the WC phase and high band contrast metrics for Co (245/255) (the metrics of the average greyscale level are given out of a full scale of 255 for the band contrast from 8 bit EBSD maps) and WC (180/255) (see Table 2).

The corresponding results for the PFIB operated at 30 kV and 59 nA are shown in Fig. 7b. Vertical top–down milling was used to prepare this surface to give fair comparison with the FIB results, as a result some curtaining can be seen which could be removed by using the rocking polishing technique described in Section 2.3. The EBSD indexing rate is only marginally worse, at 86% for the WC phase, than that recorded for the low damage BIB milling (see Table 2) with good values for WC (108/255) and excellent average band contrast for Co (220/255).

It is evident from Fig. 7c that poor results are achieved when using the Ga^+ FIB at 20 nA (30 kV). The quality of the WC EBSD patterns are degraded and are virtually unindexed (indexing only 8%) with very poor band contrast (40/255).

Fig. 7d shows that when the FIB is operated at 1 nA and 30 kV the quality of the EBSD patterns is much improved (see Table 2) being only slightly inferior to the results achieved with the PFIB operated at 59 nA current with an indexing rate in the WC phase of 76% and a band contrast average greyscale of 94/255.

With regard to the Co phase, the band contrast is only slightly worse than for BIB and PFIB, but there is some evidence (blue areas) that some regions of the Co matrix transformed from the cubic into the hexagonal phase (~ 3% HCP). The fact that different areas were mapped due to the different times taken to prepare the surfaces mean that we cannot make a quantitative comparison but it appears that the extent of transformation observed (taking into account regions that have developed during sintering [4]) in the FIB section are greater than in the PFIB and BIB datasets. It is possible that it is the chemical reactivity of the Ga^+ ions that is responsible for this transformation since this is not observed for the noble Ar and Xe beams.

From this preliminary study we have seen that in order to get equivalent results (in terms of EBSD mapping) on this material it was necessary to prepare the cross section of the WC Co sample with 1 nA using the Ga^+ FIB compared to 59 nA in the Xe^+ PFIB. The way we have assessed these results is by considering what the *maximum usable current* is in order to achieve the results required. This is somewhat difficult to describe as there are many aspects to be considered when it comes to determining what is an appropriate level of quality. As discussed in the introduction damage introduced by ion beam milling has multiple aspects to it with regards to chemical and physical interactions. As mentioned in the introduction the reactivity of Ga^+ is a clear but unquantified differentiator compared to the chemically inert Xe^+ ions. We acknowledge that we discuss the cumulative effect of damage and in reality there are several convoluted aspects to this but most notably surface amorphization, implantation and induced lattice strain. A far more detailed study is needed but is beyond the scope of this work. The results presented here thus provide a benchmark where we have found that we can utilise ~60× higher current (1 nA vs. 59 nA) to prepare surfaces of roughly equivalent quality as determined by EBSD pattern quality from band contrast and indexing rate recorded under identical conditions. We are also likely to have benefitted from an improved sputtering rate, although this has not been not quantified.

An intriguing result is that there does appear to be an influence of the current on the level of damage introduced to the specimen independent from the accelerating voltage. A current of 65 nA is available in the FIB but the resulting quality of the finished surface that means that 1 nA must be used to prepare this surface when the FIB is used. Considerable systematic work is required to map this parameter space of accelerating voltage and current for both the Ga^+ and Xe^+ milling parameters. The possibility of a chemical interaction of the Ga^+ with the WC is a clear possibility but unquantified here. Although glancing angle milling has been employed the higher current may have led to a higher dose of Ga^+ being imparted into the sample. Another possibility is that the spherical aberration which leads to the Ga^+ LMIS spot size rapidly increasingly >5 nA [32] means that even 20 nA is ineffective for preparing a cross section of this sensitive material for EBSD analysis. It is possible that the greater 'tails' on the cutting beam and a divergence from the ideal grazing incidence of the ions impinging on the cross section result in a deeper penetration and more serious physical damage. Further work is needed and custom apertures should be used to avoid limitations relating to discretization of the currents that can be used i.e. the present configuration of the PFIB provides currents of 59, 180, 470 and 1300 nA at the high end.

Table 2
Metrics from the EBSD milling, comparing the band contrast grey level and indexing rate as a function of the milling method and conditions used.

Tool	Voltage	Current	Band Contrast Average grey level		Index rate	
	(kV)	(nA)	WC	Co (fcc)	WC (%)	Co (%)
Xe^+ PFIB	30	59	108/255	220/255	~86	~92
Ga^+ FIB	30	20	40/255	190/255	~8	~91
Ga^+ FIB	30	1	94/255	210/255	~76	~93
Ar^+ BIB	6	350,000	180/255	245/255	~90	~95

3.2. Serial sectioning of WC–Co sample

Fig. 8 shows the ability of the PFIB to produce large volumetric datasets of composite materials having significant differences in hardness and crystalline structure. Fig. 8 shows a 150× 120 × 80 μm^3 3D volume of the WC–Co sample constructed from 790 slices, each 100 nm thick. The axes shown indicate the slicing direction is along the *Z*-direction and the block face is the XY plane. This WC–Co composite is composed of hard faceted WC grains (Fig. 8) and relatively soft Co grains creating a 'web-like' structure of the Co grains, typically very large in size [4]. Different orientations of the Co grains have a clearly different contrast due to electron channelling contrast (see Fig. 8b) whereas WC grains do not vary visibly in greyscale and WC–WC grain boundaries are not clearly visible. WC grains in this composition are in an energy state close to the equilibrium condition [46], thus it is expected that the facets are well defined, particularly for large WC grains. SEM images confirm this not only from the block face cut by PFIB (in Fig. 8a), but also from 'virtual sections' reconstructed at different angles (in Fig. 8b) from the data set. This indicates that PFIB is capable of precise cut positioning and milling of this sample as

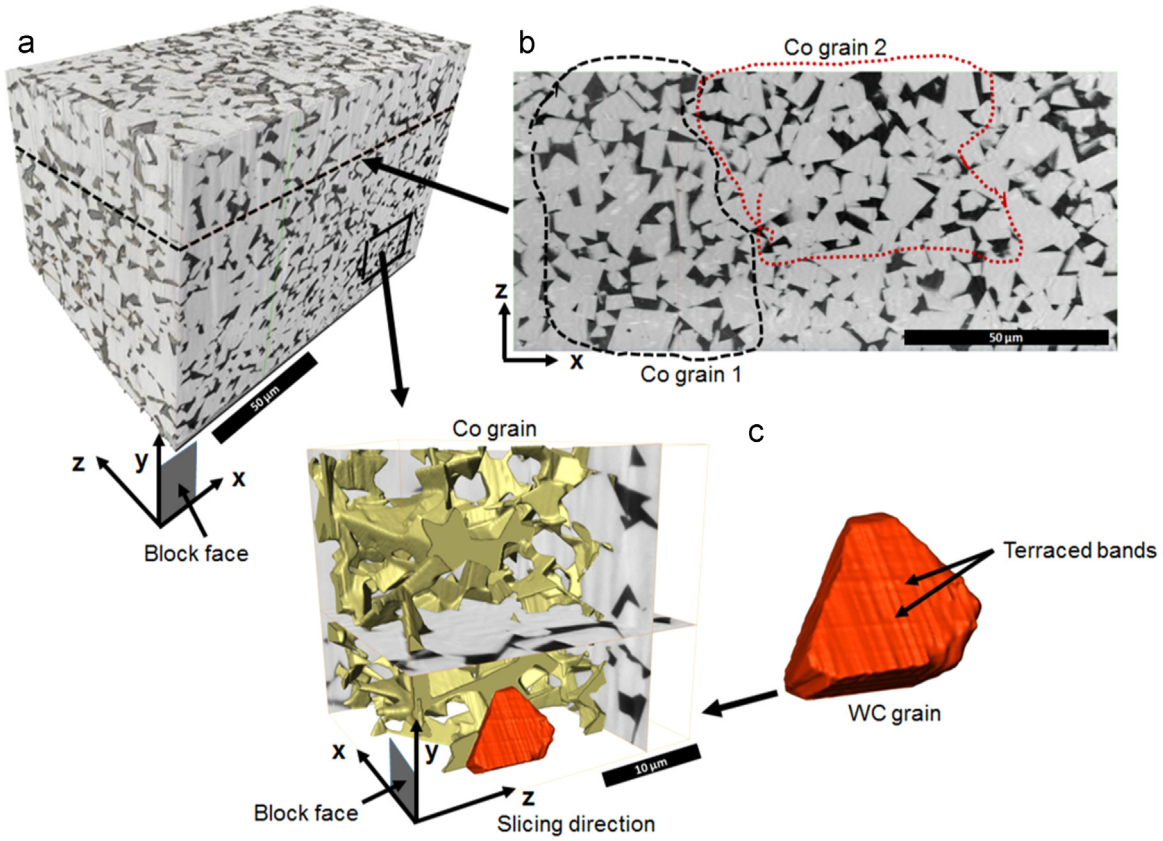

Fig. 8. (a) Reconstructed volume of WC-11% Co of 150 × 120 × 80 μm^3 prepared via SST using the PFIB at 30 kV and 59 nA, (b) shows a virtual slice in XZ plane (i.e. across all the slices, (c) shows reconstructed WC grain and a part of a single Co grain.

the analysed slices match up well and produce continuous and linear facets in all 3 dimensions. In this dataset some minor curtaining was observed during data collection but only had a marginal effect and was effectively addressed using a FFT filter (see Section 2.2). Fig. 8c shows large faceted WC grain (Note that the slicing direction, Z, is different from Fig. 8a and b). WC grains often have staircase-like bands (terraces) on the facets with a width of a few tens of nanometres. In this example two types of staircase-like features are observed. Since the voxel size of the reconstructed volume is elongated in one direction (30 × 30 × 100 nm^3) artificial staircase-like facets are clearly observed along the Z (slicing) direction and are an artefact of the serial sectioning slice not matching up perfectly. The actual terraced bands on facets with a width of a few tens of nanometres are observed as well (indicated in Fig. 8c). The artificial terraces are < 30 nm in 'height' and show a very good accuracy of the slicing and subsequent alignment such that the 'real' terraces can still be clearly observed. This is another indication that the automated SST using PFIB is capable of cutting uniformly spaced large sections, well above 100 microns across, with pixel resolution of dozens of nanometres.

3.3. A508 Grade 3 reactor pressure vessel steel sample

In this example we examined the capability of the PFIB to prepare large 3D volumes of a bainitic steel sample. Fig. 9c shows a 135 × 115 μm^2 cross section taken from a 3D image stack comprising 186 slices of 80 nm thickness (~15 μm total depth).

Fig. 10 shows a 3D representation of the voids (red) and inclusions (purple) captured within the total volume. A sub-volume was also chosen from this volume (Fig. 10) and analysed in detail

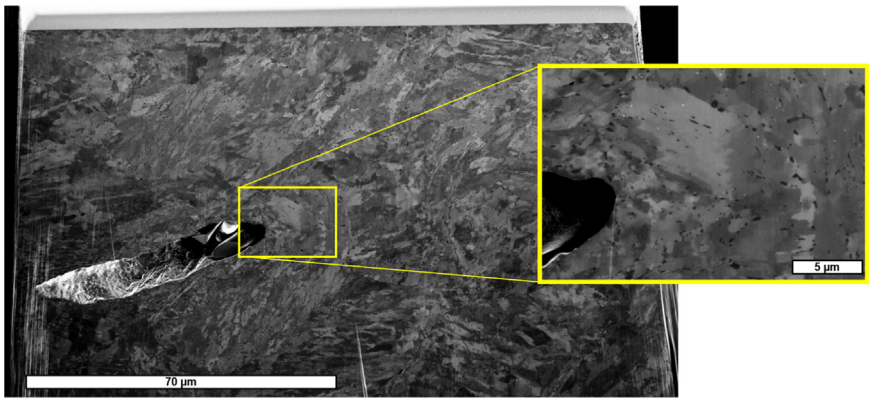

Fig. 9. SEM image of one slice recorded as part of the serial section series for the pressure vessel steel, recorded using the TLD detector at 5 kV and 0.69 nA. The horizontal field width is 160 μm and the pixel size 26 nm.

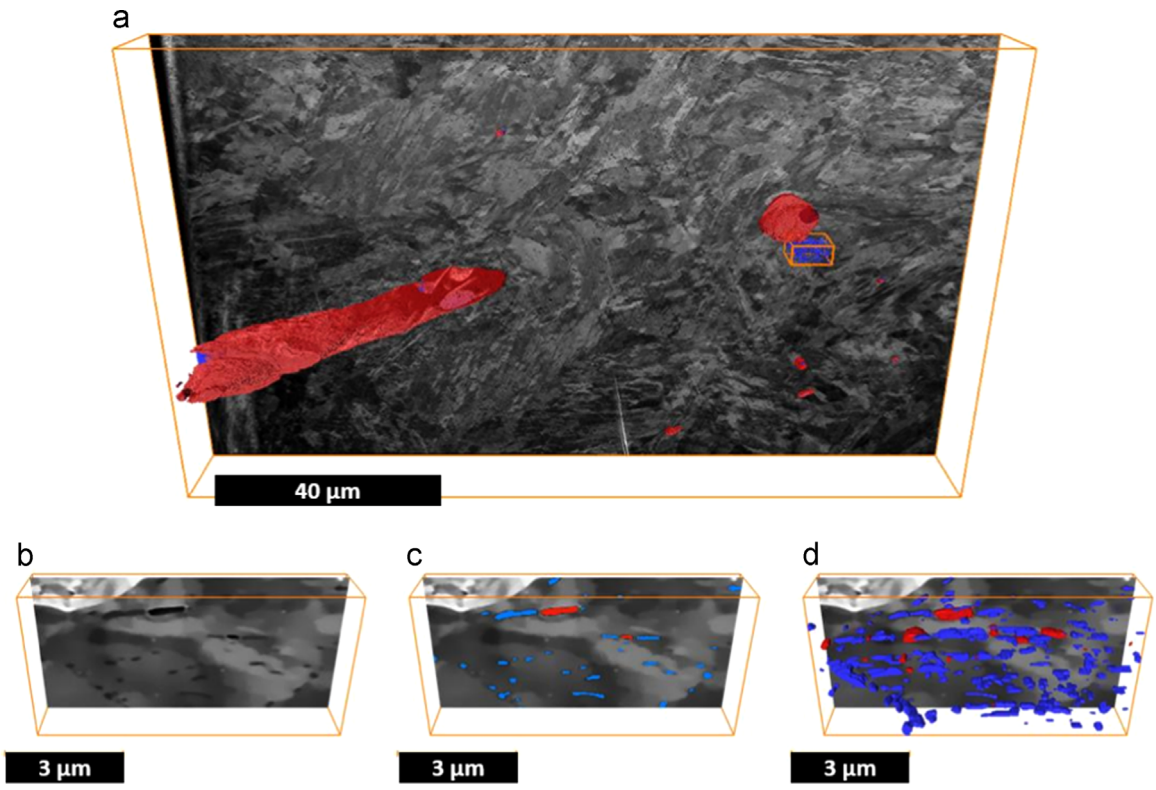

Fig. 10. An A508 Grade 3 bainitic reactor pressure vessel steel sample sectioned with FEI Helios plasma FIB-SEM at 59 nA Plasma current and 30 kV. The slice thickness is 80 nm and sectioned area is $135 \times 115\ \mu m^2$ with the pixel size of 26 nm. FEGSEM imaging at 2 kV, 0.69 nA, TLD detector in field-free mode. (a) An SEM image of the slice is shown with a visualization of the 3D voids in red and the MnS inclusions in purple. (b)SEM image of a sub-volume showing small voids and carbides, (c) carbides are labelled in blue and the voids labelled in red, (d) 3D visualization of all the carbides and voids in this sub-volume. (For interpretation of the references to color in this figure legend, the reader is referred to the web version of this article.)

in Fig. 10b–d) revealing a population of smaller voids related to the carbides. In this case the ability to observe a large 3D volume in this manner has allowed multiple voids ranging from ~100 nm to >50 μm in size to be characterized. It is clear that in each case there is an inclusion or a carbide associated with the voids and that the largest voids are typically associated with manganese sulphide (MnS) inclusions, the composition of which has been confirmed by EDX (not shown). At a finer scale 100–300 nm sized carbides are evident: these are located on lath boundaries as shown in Fig. 10b, c, d. The complex microstructure was revea-

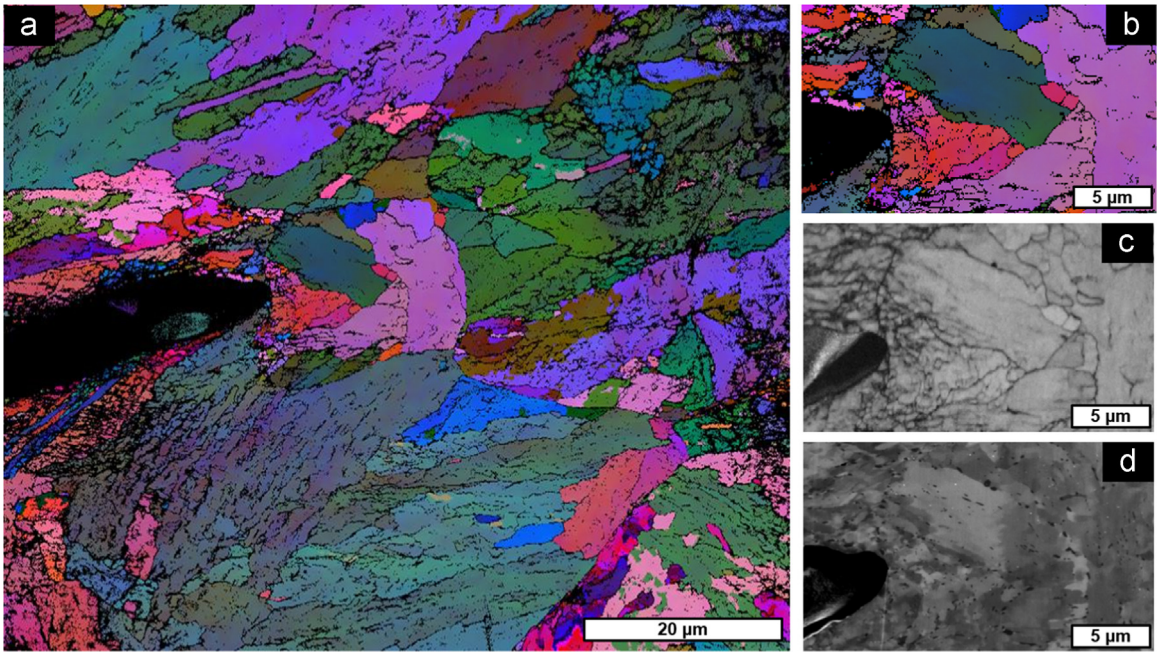

Fig. 11. Images (a) and (b) are EBSD orientation maps shown in Euler colours. A magnified region of interest taken from Fig. 9 containing the large void and the inclusion (left) and a higher resolution map of the bainitic carbide distribution (oriented to show interlath distribution) (c) a band contrast map and (d) an SE SEM image collected using an TLD detector and field-free mode. (For interpretation of the references to color in this figure legend, the reader is referred to the web version of this article.)

led with strong crystallographic electron channelling contrast allowing the relationship of the voids of different scales to be related to the microstructure. The surface finish is excellent although there is evidence of some light curtaining. As expected these curtains change direction as per the alternate direction employed in the rocking mill. The limited size and clearly defined boundaries of the regions most affected by curtaining suggest that these were regions of similar crystallographic orientation. These light curtains (i.e. no black or white signal saturation) were effectively removed by post processing and have negligible impact on the ability to identify the different microstructural features.

Fig. 11 shows EBSD results from the final slice of the same reactor pressure vessel volume. The resulting EBSD dataset shown in Fig. 11a shows very high levels of indexing (~89%). It is clear from Fig. 11c that the surface quality (band contrast) is excellent despite the very fast milling rate (59 nA at 30 kV). Indeed, it appears that most of the non-indexed points are associated with grain and subgrain boundaries and the edges of the mapped area, which experienced some shadowing.

3.3.1. Concluding remarks

Emerging plasma Xe^+ PFIB-SEM technology offers the promise of a fast and low damage means of milling samples at high rates and with considerable flexibility. Based on the concept of *maximum usable current* for the SST with dual beams, our results have shown that Plasma Xe^+ FIBs are capable of material removal rates some 60× greater than conventional Ga^+ FIB systems with comparable or less damage. To date there is very little established literature on the use of Xe^+ PFIBs for milling and serial sectioning and hence the optimisation of the milling procedures is still very much in its infancy. It is possible that with further process optimisation it may be possible to push the milling currents yet higher and also improve the quality at a given current. More work remains to be done to assure the flatness and parallel nature of serial sections but the preliminary results look very promising. The point at which the Xe^+ PFIB becomes preferable for milling duties compared to the Ga^+ FIB appears to be at slightly lower currents than previously thought but is in the tens of nA range. The deconvolution of the different aspects of physical and chemical damage to understand the different results achieved using the Ga^+ compared to the Xe^+ beam chemistries remains a challenge that would merit quantification.

Further work remains to establish the optimal and the acceptable (faster) milling conditions for a wide range of materials. To date we have examined several Al, Ni, Co alloys, ferritic and austenitic steels, paint, WC, olivine, device materials and dentin all with good results although the conditions must be tailored specifically for each material. Going forward it will also be important to establish the levels of implantation damage or residual stress introduced by Xe^+ PFIB milling along the lines of research already carried out for conventional FIB [47]. Our preliminary results seem to suggest that the levels of damage are lower despite the higher milling currents.

While the use of FIB-SEMs to address materials issues has been widespread over the last 10 years, the volumes accessible via serial sectioning to produce 3D images within reasonable timescales have been frustratingly small. In many cases an analysed volume of only tens of microns means that the VoI contains few grains or grain boundaries. With volumes potentially 1000× greater recorded in practical timescales it looks like the PFIB will overcome this issue. There is much work to be done to understand how different materials behave under milling by the PFIB and it is certain some new strategies will need to be developed.

In view of the faster materials removal rates, the Xe^+ PFIB-SEM can act as a critical link between non-destructive X-ray imaging methods and destructive serial sectioning methods within a correlative tomography framework, as recently proposed [19]. There are many cases where micron-sized features of importance that lie hundreds of microns beneath the surface can be identified and located by microscale X-ray CT for subsequent excavation by PFIB either for subsequent non-destructive examination in more detail by nanoscale X-ray CT [48,49] or for subsequent large volume serial sectioning possible in the PFIB-SEM itself or for higher resolution TEM. Further, there is interest in excavating small volumes of interest for mechanical evaluation. Such a VoI which might incorporate an inclusion say, or might be taken from a near surface white layer, hydrogen embrittled region or radiation exposed surface layer for subsequent micro-testing and performance evaluation either as pillars [50,51], cantilevers [52,53] or tensile test-pieces [54].

Of course other issues remain with respect to the collection of 3D datasets; most obviously the acquisition time and the computer resources required to store, analyse and visualise high resolution 3D datasets. This may well require a smarter approach to the collection of such data because while it may take several minutes to mill a $200 \times 200\ \mu m^2$ slice in the PFIB it takes significantly longer to collect an EBSD image or an EDX map at high resolution over that area. This problem becomes very significant if 3D EBSD or 3D EDX maps are required. Nevertheless initial indications suggest that emerging Xe^+ PFIBs could significantly extend the capability of 3D destructive serial sectioning.

Acknowledgements

We acknowledge the EPSRC for Grants EP/J021229/1 and EP/M010619/1 and UK Research Partnership Investment Funding that established the Multiscale Characterisation Facility. We gratefully acknowledge Trisha Rice, Kenny Mani and Remco Geurts at FEI for their support during this work. Authors acknowledge NPL for supply of WC–Co samples.

References

[1] F. Tariq, R. Haswell, P.D. Lee, D.W. McComb, Characterization of hierarchical pore structures in ceramics using multiscale tomography, Acta Mater. 59 (5) (2011) 2109–2120.
[2] J. Burrell, R.S. Bradley, S. Walker-Samuel, Y. Jamin, L.C.J. Baker, J.K.R. Boult, P. J. Withers, J. Halliday, J.C. Waterton, S.P. Robinson, MRI measurements of vessel calibre in tumour xenografts: comparison with vascular corrosion casting, Microvasc. Res. 84 (3) (2012) 323–329.
[3] T. Hashimoto, X. Zhou, C. Luo, K. Kawano, G.E. Thompson, A.E. Hughes, P. Skeldon, P.J. Withers, T.J. Marrow, A.H. Sherry, Nanotomography for understanding materials degradation, Scr. Mater. 63 (8) (2010) 835–838.
[4] K. Mingard, B. Roebuck, J. Marshall, G. Sweetman, Some aspects of the structure of cobalt and nickel binder phase in hardmetals, Acta Mater. (2011) 2277–2290.
[5] T. Lowe, R.J. Garwood, T.J. Simonsen, R.S. Bradley, P.J. Withers, Metamorphosis revealed: time-lapse three-dimensional imaging inside a living chrysalis, J. R. Soc. Interface 10 (84) (2013).
[6] E. Maire, P.J. Withers, Quantitative X-ray tomography, Int. Mater. Rev. 59 (1) (2014) 1–43.
[7] J. Spowart, Automated serial sectioning for 3-D analysis of microstructures, Scr. Mater. 55 (1) (2006) 5–10.
[8] G. Thompson, T. Hashimoto, X.L. Zhong, M. Curioni, X. Zhou, P. Skeldon, P. J. Withers, J.A. Carr, A.G. Monteith, Revealing the three dimensional internal structure of aluminium alloys, Surf. Interface Anal. 45 (10) (2013) 1536–1542.
[9] M. Echlin, A. Mottura, C. Torbet, T.M. Pollock, A new tribeam system for three-dimensional multimodal materials analysis, Rev. Sci. Instrum. 83 (2) (2012) 023701.
[10] B. Winiarski, A. Gholinia, K. Mingard, M. Gee, G. Thompson, P.J. Withers, Quantitative large volume 3-D EBSD, manuscript in preparation.
[11] B. Winiarski, A. Gholinia, K. Mingard, M. Gee, G. Thompson, P.J. Withers, Broad Ion Beam Serial Section Tomography, manuscript in preparation.
[12] I. Borgh, P. Hedström, J. Odqvist, A. Borgenstam, J. Agren, A. Gholinia, B. Winiarski, P.J. Withers, G.E. Thompson, K. Mingard, M.G. Gee, On the three-dimensional structure of WC grains in cemented carbides, Acta Mater. 61 (2013) 4726–4733.

[13] M. Groeber, B.K. Haley, M.D. Uchic, D.M. Dimiduk, S. Ghosh, 3D reconstruction and characterization of polycrystalline microstructures using a FIB-SEM system, Mater. Charact. 57 (4–5) (2006) 259–273.
[14] P. Midgley, R.E. Dunin-Borkowski, Electron tomography and holography in materials science, Nat. Mater. 8 (4) (2009) 271–280.
[15] T. Slater, A. Macedo, S.L.M. Schroeder, M.G. Burke, P. O'Brien, P.H.C. Camargo, S. J. Haigh, Correlating catalytic activity of Ag–Au nanoparticles with 3D compositional variations, Nano Lett. 14 (4) (2014) 1921–1926.
[16] K. Thompson, D. Lawrence, D.J. Larson, J.D. Olson, T.F. Kelly, B. Gorman, In situ site-specific specimen preparation for atom probe tomography, Ultramicroscopy 107 (2–3) (2007) 131–139.
[17] T. Kelly, M.K. Miller, Invited review article: atom probe tomography, Rev. Sci. Instrum. 78 (3) (2007).
[18] M. Cantoni, L. Holzer, Advances in 3D focused ion beam tomography, MRS Bull. 39 (4) (2014) 354–360.
[19] T. Burnett, S.A. McDonald, A. Gholinia, R. Geurts, M. Janus, T. Slater, S.J. Haigh, C. Ornek, F. Almuaili, D.L. Engelberg, G.E. Thompson, P.J. Withers, Correlative tomography, Sci. Rep. 4 (2014) 4711.
[20] J. Caplan, M. Niethammer, R.M.I.I. Taylor, K.J. Czymmek, The power of correlative microscopy: multi-modal, multi-scale, multi-dimensional, Curr. Opin. Struct. Biol. 21 (5) (2011) 686–693.
[21] W. Lenthe, Mc.L.P. Echlin, A. Trenkle, M. Syha, P. Gumbsch, T.M. Pollock, Quantitative voxel-to-voxel comparison of TriBeam and DCT strontium titanate three-dimensional data sets, J. Appl. Crystallogr. 48 (2015) 1034–1046.
[22] C. Rue, B. Carrigan, Dielectric and metal depositions using Xe^+ focused ion beams, in: Istfa 2012: Conference Proceedings from the 38th International Symposium for Testing and Failure Analysis, 2012, pp. 447–454.
[23] F. Altmann, S. Klengel, J. Schischka, M. Petzold, Defect analysis using high throughput plasma fib in packaging reliability investigations, in: IEEE 63rd Electronic Components and Technology Conference (ECTC), 2013, pp. 1940–1945.
[24] F. Altmann, R.J. Young, Site-specific metrology, inspection, and failure analysis of three-dimensional interconnects using focused ion beam technology, J. Micro-Nanolithogr. Mems Moems 13 (1) (2014).
[25] L. Kwakman, F. German, M. Maaike, T. Visser, A. Klumpp, P. Ramm, Characterization and failure analysis of 3D integrated systems using a novel plasma-FIB system, Front. Charact. Metrol. Nanoelectron. 2011 (2011) 1395.
[26] N.S. Smith, W.P. Skoczylas, S.M. Kellogg, D.E. Kinion, P.P. Tesch, O. Sutherland, A. Aanesland, R.W. Boswell, High brightness inductively coupled plasma source for high current focused ion beam applications, J. Vaccum Sci. Technol. B 24 (6) (2006) 2902–2906.
[27] M.M.V. Taklo, A. Klumpp, P. Ramm, L. Kwakman, G. Franz, Bonding and TSV in 3D IC integration: physical analysis with a plasma FIB, Microsc. Anal. 25 (7) (2011) 9–12.
[28] T. Hrnčíř, J. Dluhoš, L. Hladík, E. Moyal, J. Teshima, J. Kopeček, Advances in FIB-SEM analysis of TSV and solder bumps-approaching higher precision, throughput, and comprehensiveness, in: ISTFA 2014: The 40th International Symposium for Testing and Failure Analysis, ASM International Houston, Texas, USA, 2014.
[29] J. Jiruše, T. Hrnčíř, F. Lopour, M. Zadražil, A. Delobbe, O. Salord, Combined plasma FIB-SEM, Microsc. Microanal. 18 (2) (2012) S652–S653.
[30] N. Bassim, K. Scott, L.A. Giannuzzi, Recent advances in focused ion beam technology and applications, MRS Bull. 39 (4) (2014) 317–325.
[31] I.G. Brown, The Physics and Technology of Ion Sources, Wiley, New York, 1989.
[32] N. Smith, W.P. Skoczylas, S.M. Kellogg, D.E. Kinion, P.P. Tesch, O. Sutherland, A. Aanesland, R.W. Boswell, High brightness inductively coupled plasma source for high current focused ion beam applications, J. Vaccum Sci. Technol. B 24 (6) (2006) 2902–2906.
[33] J.F. Ziegler, J.P. Biersack, U. Littmark, The Stopping Range of Ions in Matter, Pergamon Press, New York, 1985.
[34] J.F. Ziegler, SRIM-2003, vol. 219–220, 2004, p. 1036.
[35] R. Kelley, K. Song, B. Van Leer, D. Wall, L. Kwakman, Xe^+ FIB milling and measurement of amorphous silicon damage, Microsc. Microanal. 19 (S2) (2013) 862–863.
[36] V. Randle, O. Engler, Introduction to Texture Analysis: Macrostructure, Microtexture and Orientation Mapping, 2nd Edition, CRC Press, Boca Raton, 2009.
[37] J. Michael, Focussed ion beam induced microstructural alterations: texture development, grain growth and intermetallic formation, J. Microsc. Microanal. 17 (2011) 386–397.
[38] C. Ransley, D.E.J. Talbot, The embrittlement of aluminium magnesium alloys by sodium, J. Inst. Met. 88 (4) (1959) 150–158.
[39] D. Talbot, C.E. Ransley, Addition of bismuth to aluminum–magnesium alloys to prevent embrittlement by sodium, Metall. Trans. A – Phys. Metall. Mater. Sci. 8 (7) (1977) 1149–1154.
[40] B. Kempshall, L.A. Giannuzzi, B.I. Prenitzer, F.A. Stevie, S.X. Da, Comparative evaluation of protective coatings and focused ion beam chemical vapor deposition processes, J. Vaccum Sci. Technol. B 20 (1) (2002) 286–290.
[41] S. Bals, W. Tirry, R. Geurts, Z. Yang, D. Schryvers, High-quality sample preparation by low kV FIB thinning for analytical TEM measurements, Microsc. Microanal. 13 (2) (2007) 80–86.
[42] S. Kellogg, R. Schampers, S.Y. Zhang, A.A. Graupera, T. Miller, D.W. Laur, A. B. Dirriwachter, High throughput sample preparation and analysis using an Inductively Coupled Plasma (ICP) focused ion beam source, J. Microsc. Microanal. 16 (2) (2010) 222–223.
[43] V. Sarin, T. Johannesson, On the deformation of WC–Co cemented carbides, Met. Sci. 9 (1975) 472–476.
[44] M. Daly, F. Leonard, A. Sherry, Application of 3D X-ray tomography to enhance the calibration of ductile fracture models' in: Asme 2014 Pressure Vessels & Piping Conference PVP, 2014.
[45] T. Burnett, R. Geurts, H. Jazaeri, S.M. Northover, S.A. McDonald, S.J. Haigh, P. J. Bouchard, P.J. Withers, Multiscale 3D analysis of creep cavities in AISI type 316 stainless steel, Mater. Sci. Technol. 31 (5) (2015) 522–534.
[46] B. Roebuck, C. Phatak, I. Birks-Agnew, A comparison of the linear intercept and equivalent circle methods for grain size measurement in WC/Co hardmetals, report MATC(A)149, NPL, London, 2004.
[47] M. Rommel, G. Spoldi, V. Yanev, S. Beuer, B. Amon, J. Jambreck, S. Petersen, A. J. Bauer, L. Frey, Comprehensive study of focused ion beam induced lateral damage in silicon by scanning probe microscopy techniques, J. Vaccum Sci. Technol. B 28 (3) (2010) 595–607.
[48] D.S. Eastwood, R.S. Bradley, F. Tariq, S.J. Cooper, O.O. Taiwo, J. Gelb, A. Merkle, D.J.L. Brett, N.P. Brandon, P.J. Withers, P.D. Lee, P.R. Shearing, The application of phase contrast X-ray techniques for imaging Li-ion battery electrodes, Nucl. Instrum. Methods Phys. Res. Sect. B-Beam Interact. Mater. Atoms 324 (2014) 118–123.
[49] P.R. Shearing, R.S. Bradley, J. Gelb, S.N. Lee, A. Atkinson, P.J. Withers, N. P. Brandon, Using synchrotron X-Ray nano-CT to characterize SOFC electrode microstructures in three-dimensions at operating temperature, Electrochem. Solid State Lett. 14 (10) (2011) B117–B120.
[50] T. Csanadi, M. Bl'anda, A. Duszova, N.Q. Chinh, P. Szommer, J. Dusza, Deformation characteristics of WC micropillars, J. Eur. Ceram. Soc. 34 (15) (2014) 4099–4103.
[51] D. Kaufmann, A.S. Schneider, R. Monig, C.A. Volkert, O. Kraft, Effect of surface orientation on the plasticity of small bcc metals, Int. J. Plast. 49 (2013) 145–151.
[52] M.G. Mueller, V. Pejchal, G. Zagar, A. Singh, M. Cantoni, A. Mortensen, Fracture toughness testing of nanocrystalline alumina and fused quartz using chevron-notched microbeams, Acta Mater. 86 (2015) 385–395.
[53] M. Trueba, A. Aramburu, N. Rodriguez, I. Iparraguirre, M.R. Elizalde, I. Ocana, J. M. Sanchez, J.M. Martinez-Esnaola, "In-situ" mechanical characterisation of WC–Co hardmetals using microbeam testing, Int. J. Refract. Met. Hard Mater. 43 (2014) 236–240.
[54] K. Fujii, K. Fukuya, Development of micro tensile testing method in an FIB system for evaluating grain boundary strength, Mater. Trans. **52** (1) (2011) 20–24.